Landslide generated impulse waves

2. Hydrodynamic impact craters

Journal Article

Author(s):
Fritz, H.M.; Hager, Willi H.; Minor, H.-E.

Publication date:
2003-12

Permanent link:
https://doi.org/10.3929/ethz-b-000052797

Originally published in:
Experiments in Fluids 35(6), https://doi.org/10.1007/s00348-003-0660-7

Experiments in Fluids 35 (2003) 520–532
DOI 10.1007/s00348-003-0660-7

Landslide generated impulse waves. 2. Hydrodynamic impact craters

H.M. Fritz, W.H. Hager, H.-E. Minor

Abstract Landslide generated impulse waves were investigated in a two-dimensional physical laboratory model based on the generalized Froude similarity. Digital particle image velocimetry (PIV) was applied to the landslide impact and wave generation. Areas of interest up to 0.8 m by 0.8 m were investigated. PIV provided instantaneous velocity vector fields in a large area of interest and gave insight into the kinematics of the wave generation process. Differential estimates such as vorticity, divergence, and elongational and shear strain were extracted from the velocity vector fields. At high impact velocities flow separation occurred on the slide shoulder resulting in a hydrodynamic impact crater, whereas at low impact velocities no flow detachment was observed. The hydrodynamic impact craters may be distinguished into outward and backward collapsing impact craters. The maximum crater volume, which corresponds to the water displacement volume, exceeded the landslide volume by up to an order of magnitude. The water displacement caused by the landslide generated the first wave crest and the collapse of the air cavity followed by a run-up along the slide ramp issued the second wave crest. The extracted water displacement curves may replace the complex wave generation process in numerical models. The water displacement and displacement rate were described by multiple regressions of the following three dimensionless quantities: the slide Froude number, the relative slide volume, and the relative slide thickness. The slide Froude number was identified as the dominant parameter.

Received: 25 November 2002 / Accepted: 2 June 2003

H.M. Fritz (✉), W.H. Hager, H.-E. Minor
Hydrology and Glaciology (VAW), Laboratory of Hydraulics,
Swiss Federal Institute of Technology (ETH),
8092 Zurich, Switzerland
E-mail: hermann.fritz@gtrep.gatech.edu
Tel.: +1-912-9667947
Fax: +1-912-9667836

H.M. Fritz
Present address: Georgia Institute of Technology,
210 Technology Circle, Savannah, GA31407, USA

The research work presented was supported by the Swiss National Science Foundation, grant number 2100-050586.97. The whole PIV system was generously funded by an extraordinary credit issued by the Swiss Federal Institute of Technology (ETH).

List of symbols

a	wave amplitude (L)
b	slide width (L)
c	wave celerity (LT^{-1})
d_g	granulate grain diameter (L)
d_p	seeding particle diameter (L)
$\mathbf{F}$	slide Froude number
g	gravitational acceleration (LT^{-2})
h	stillwater depth (L)
H	wave height (L)
l_s	slide length (L)
L	wave length (L)
M	magnification
m_s	slide mass (M)
n_{por}	slide porosity
Q_d	water displacement rate (L^3)
Q_D	maximum water displacement rate (L^3)
Q_s	maximum slide displacement rate
s	slide thickness (L)
S	relative slide thickness
t	time after impact (T)
t_D	time of maximum water displacement volume (L^3)
t_{qD}	time of maximum water displacement rate (L^3)
t_{si}	slide impact duration (T)
t_{sd}	duration of subaqueous slide motion (T)
T	wave period (T)
v	velocity (LT^{-1})
v_p	particle velocity (LT^{-1})
v_{px}	streamwise horizontal component of particle velocity (LT^{-1})
v_{pz}	vertical component of particle velocity (LT^{-1})
v_s	slide centroid velocity at impact (LT^{-1})
V	dimensionless slide volume
V_d	water displacement volume (L^3)
V_D	maximum water displacement volume (L^3)
V_s	slide volume (L^3)
x	streamwise coordinate (L)
z	vertical coordinate (L)
α	slide impact angle (°)
δ	bed friction angle (°)
Δx	mean particle image x-displacement in interrogation window (L)
$\epsilon_{\Delta x}$	random displacement Δx error (L)
ϵ_{tot}	total random velocity v error (LT^{-1})
ϵ_{xx}	streamwise horizontal elongational strain component (1/T)
ϵ_{xz}	shear strain component (1/T)
ϵ_{zx}	shear strain component (1/T)
ϵ_{zz}	vertical elongational strain component (1/T)

η	water surface displacement (L)
ρ	density (ML^{-3})
ρ_g	granulate density (ML^{-3})
ρ_p	particle density (ML^{-3})
ρ_s	mean slide density (ML^{-3})
ρ_w	water density (ML^{-3})
φ'	granulate internal friction angle (°)
ω_y	vorticity vector component (out-of-plane) (1/T)

1
Introduction

Large water waves may be generated by landslides, shore instabilities, snow avalanches, and glacier and rock falls in geometrically confined water bodies such as reservoirs, lakes, and bays (Slingerland and Voight 1979). For Alpine lakes impulse waves are particularly significant, because of steep shores, narrow reservoir geometries, possible large slide masses, and high impact velocities. The resulting impulse waves can cause disaster caused by run-up along the shoreline and overtopping of dams (Vischer and Hager 1998). The focus of the present study is on the wave generation process, the near field wave propagation, and in particular the water displacement in a two-dimensional physical model. The radial wave propagation in a three-dimensional physical model was investigated by Huber (1980) and the wave run-up is referred to in Müller (1995). Subaerial rockslide impacts into water bodies with the subsequent wave generation and propagation were considered in a two-dimensional Froude similarity model. The recorded wave profiles were extremely unsteady and non-linear. Four wave types were determined: weakly non-linear oscillatory wave, non-linear transition wave, solitary-like wave, and dissipative transient bore (Fritz 2002b). Most of the generated impulse waves were located in the intermediate water depth wave regime. The physical model results were compared to the giant rockslide generated impulse wave, which struck the shores of the Lituya Bay, Alaska, in 1958. The measurements obtained in the physical model were in agreement with the in-situ data (Fritz et al. 2001). This paper focuses on the landslide impact induced water displacement volumes and rates extracted from the instantaneous velocity vector fields obtained by particle image velocimetry (PIV).

2
Experimental set-up

2.1
Physical model

The granular rockslide impact experiments were conducted in a rectangular prismatic water wave channel (L×W×H=11 m×0.5 m×1 m) with varying stillwater depths h=0.30, 0.45, and 0.675 m. At the front end of the channel a 3-m long hill slope ramp was built into the channel at an angle α=45°. The landslides were modeled with an artificial granular material characterized in Fritz et al. (2003). The dynamic slide impact characteristics were controlled by means of a novel pneumatic landslide generator (Fritz and Moser 2003). The following four relevant parameters governing the wave generation were varied: granular slide mass m_s, slide impact velocity v_s, stillwater depth h, and slide thickness s. The parameters to describe impulse waves were introduced in Fritz et al. (2003). The notation is recalled: slide thickness s, slide length l_s, slide centroid velocity v_s at impact, slide density ρ_s, still water depth h, hill slope angle α, streamwise coordinate x, vertical coordinate z, wave propagation velocity c, wavelength L, wave period T, wave height H, amplitude a, time after impact t, water surface displacement $\eta(t)$. The main wave characteristics were related to the following three dimensionless quantities: the slide Froude number $F = v_s/\sqrt{gh}$, the dimensionless slide volume $V=V_s/(bh^2)$, and the dimensionless slide thickness $S=s/h$. The investigated ranges were discussed in Fritz et al. (2003).

2.2
Instrumentation

Three different measurement techniques were built into the physical model: laser distance sensors (LDS), PIV, and capacitance wave gages (CWG). The granular slide profiles were scanned in the channel axis before impact with two laser distance sensors (LDS). The wave features in the propagation area were determined with capacitance wave gages (CWG). The PIV system consisted of a twin cavity Nd-YAG laser as the light source and a full-frame progressive-scan interline transfer CCD camera (Fritz 2002a). The optical configuration and the properties of the seeding particles were discussed in Fritz et al. (2003). The instantaneous 2D–2C velocity vector fields were computed with a cross-correlation based adaptive multi-pass algorithm (Scarano and Riethmuller 2000). The absolute measurement error of a single displacement vector was determined to $\epsilon_{tot} \leq 0.07$ m/s with a conservative assumption for the random displacement error $\epsilon_{\Delta x}$=0.1 pixel (Fritz et al. 2003). PIV provided instantaneous velocity vector fields in the slide impact area and gave insight into the kinematics of wave generation. A total of 137 experimental runs were conducted (Fritz 2002b). In some cases juxtaposed areas of view were acquired in repeated experiments (Fritz et al. 2003). The applied standard planar PIV provided the v_{px} and v_{pz} components of the particle velocity vector v_p and its differentials in the x and z directions (Raffel et al. 1998). The following terms of the deformation tensor were computed: the in-plane divergence $\epsilon_{xx}+\epsilon_{zz}$, the out-of-plane vorticity component ω_y, the elongational strain rate $\epsilon_{xx}-\epsilon_{zz}$, and the shear strain rate ϵ_{xz} (Fritz et al. 2003).

3
Hydrodynamic impact craters

3.1
Flow separation

A hydrodynamic impact crater formed when flow separation occurred. Flow separation was defined by the occurrence of a water body detachment on the back of the slide. This definition was used to classify all of the experiments conducted into separated and unseparated flows. Characteristic examples of an unseparated and a separated flow around penetrating landslides are shown in Fig. 1a and b, respectively. The separation point accompanied by a detachment of the water body was typically located on the slide shoulder as shown in Fig. 1b.

The examples shown in Fig. 1 demonstrate a strong influence of the flow separation on the displaced water volume. The only significant difference between the two experiments was the impact Froude number. The water displacement at very low slide impact velocities $\mathbf{F} \ll 1$ may approach the asymptotic water displacement volume given by the slide volume added to the water body. The water displacement was similar to the landslide volume at $\mathbf{F}=1.4$ shown in Fig. 1a. Only a minor addition was due to the trough formed on the back and in the wake of the slide. The detachment of the water body on the slide shoulder at $\mathbf{F}=2.6$ shown in Fig. 1b caused a hydrodynamic impact crater. The displaced water volume obviously exceeded the landslide volume significantly. Instantaneous flow field sequences of a landslide impact without flow separation at $\mathbf{F}=1.7$ and an example with flow separation at $\mathbf{F}=4.1$ were presented in Fritz et al. (2003).

The flow separation always initiated on the inclined ramp with locally reduced water depths and accordingly lower shallow water wave propagation velocities. Nevertheless the slide Froude number lent itself as primary classification parameter, which was defined using the still water depth h of the wave tank. Flow separation was always observed if the slide Froude number $F = v_s / \sqrt{gh}$ satisfied the empirical relationship

$$F > \left(\frac{5}{3} + \frac{1}{2} S \right) \tag{1}$$

with the relative slide thickness $S=s/h$. The water depth at the actual point of separation on the ramp was smaller and therefore also the water displacement under the wave crest would be reduced. Noteworthy is the analogy of the first term in the separation criterion given by inequality (1) to the formation of roll waves determined by the Vedernikov number (Liggett 1994). The graphical representation of inequality (1) is shown in Fig. 2.

The separation criterion defined in (1) indicates a slight increase in the Froude number at which separation occurred with the relative slide thickness $S=s/h$. A thick slide continuously built up its thickness from the front to the maximum slide thickness, whereas thin slides quickly reached a plateau in slide thickness. Local flow separations at impact with immediate reattachment of the flow on the back of the slide occurred in some cases below the limit defined in (1). The water displacement volume during local flow separations did not exceed the landslide volume. Hence their effect on the wave generation process is secondary. The landslide may be considered as a moving wall if the slide thickness significantly exceeds the water depth. No flow over the back of the landslide and therefore no flow separation would occur if $S \gg 1$. The maximum dimensionless discharge per unit width equals $\mathbf{F} \cdot S$, but did not result in an improved classification.

3.2
Hydrodynamic impact crater regimes

In general the drop of objects, from small droplets to large hypothetical meteorites in the ocean, or man-made underwater explosions are phenomena causing impact craters or cavities that ultimately collapse and form a rebound as a vertical spike or dome reaching considerable height above the still water surface (Holst 1977).
A hydrodynamic impact crater may only form if flow separation on the slide shoulder occurs. Hence hydrodynamic impact cratering is of importance if the slide Froude number is within the separated flow region defined by (1). The dominant mechanism governing the formation of the hydrodynamic impact crater is the transfer of the kinetic energy from the mass flow to the fluid. This energy transfer is driven by the dissipative processes associated with drag on the landslide. An analytical model specified the energy transfer for cavity production as equivalent to the energy dissipated by velocity-dependent drag on the water-entering object (Lee et al., 1997). As a landslide penetrates the free surface, the impact crater expands until the difference between the pressure in the surrounding fluid and that in the crater balances the induced inertial effects and drives the fluid back towards its undisturbed state. The ensuing crater collapse can lead to a closure resulting in the formation of an instantaneous cavity (Birkhoff and Zarantonello 1957). With the occurrence of a closure it is possible to distinguish between backward and outward collapsing craters. The impact velocity and the shape of the landslide are the critical parameters. Hence the ranges of occurrence of the different crater types were defined in analogy to the flow separation criterion. An outward collapsing water crater was always observed if the slide Froude number $\mathbf{F}=v_s/(gh)^{0.5}$ satisfied the empirical relationship

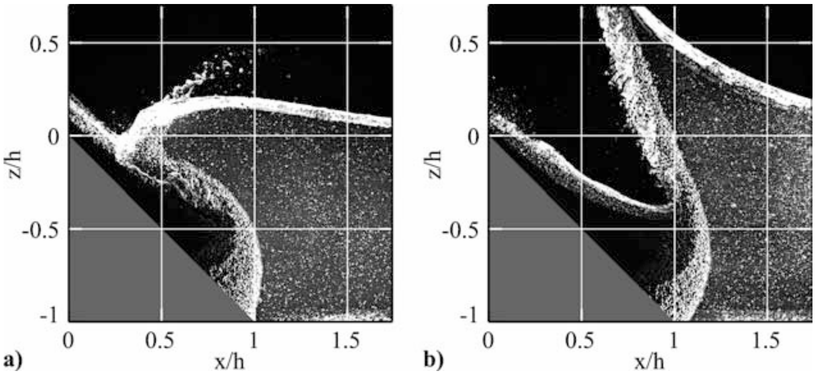

Fig. 1a, b. Flow separation on the slide shoulder at $h=0.45$ m. **a** unseparated flow at $\mathbf{F}=1.4$, $V=0.35$, $S=0.23$ and $t(g/h)^{0.5}=1.13$; **b** separated flow at $\mathbf{F}=2.6$, $V=0.35$, $S=0.21$ and $t(g/h)^{0.5}=0.79$

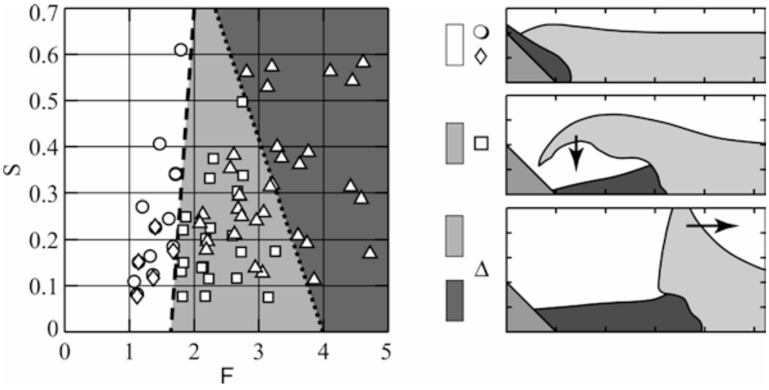

Fig. 2. Flow separation and crater type formation: slide thickness $S=s/h$ vs. slide Froude number $\mathbf{F}=v_s/(gh)^{0.5}$ with: *open circle*, no flow separation; *open diamond*, local flow separation; *open square*, backward collapsing impact craters; *open triangle*, outward collapsing impact craters, *long dashes*, Eq. (1), *short dashes*, Eq. (2), *light grey*, complex transition region with backward and outward collapsing craters, *dark grey*, only outward collapsing craters

$$F>\left(4-\frac{5}{2}S\right). \tag{2}$$

Both crater collapse types were observed in the complex transition region delimited by (1) and (2) resulting in

$$\left(\frac{5}{3}+\frac{1}{2}S\right)\leq F\leq\left(4-\frac{5}{2}S\right). \tag{3}$$

These observed water crater collapse regimes are shown in Fig. 2 together with the criterion for flow separation. The transition from backward to outward collapsing impact craters is highly complex. A deep closure was often observed at the transition resulting in a partial reattachment of the crater boundary on the back of the slide. A deep closure did not cause a significant inclusion of air pockets. The whole upper cavity wall collapsed outward. Therefore cases with a deep closure were also classified as outward collapsing impact craters. Most relevant events of landslide generated impulse waves were observed within the Froude number range $0.5<\mathbf{F}<4$ (Slingerland and Voight 1979). Hence unseparated and separated flows as well as backward and outward collapsing impact craters are expected to occur in real events.

3.3
Backward collapsing impact crater

A characteristic example of a backward collapsing hydrodynamic crater formed by a landslide impact at $\mathbf{F}=2.8$ is shown in Fig. 3. The set of figures includes the original PIV images, the velocity vector field, scalar fields of the velocity components, and contour plots of computed components of the deformation tensor. The selected sequence of original PIV recordings is shown Fig. 3A. The water flow around the penetrating landslide separated on the slide shoulder (Fig. 3Aa,b). The water was initially expelled upwards and outward by the entry of the landslide forming a water crater. The water crater exposed the ramp and the back of the landslide to the atmosphere. The displaced water volume obviously exceeded the landslide volume significantly. As the process of crater growth has terminated outward bulk motion of water was still present as a residuum. The uplift evolved into a leading wave. The backward collapsing impact crater was governed by a surface closure resulting in the inclusion of air pockets in the form of a cavity (Fig. 3Ac,d). The amount of air inclusion strongly depended on the cavity type. The largest air volumes were entrained by backward collapsing impact craters owing to the early surface closure. The subsequent cavity collapse and the resulting rebound issued an almost vertical jet (Fig. 3Ae,f). A considerable portion of the energy imparted to the fluid is lost as a result of turbulent mixing at the impact site and the jet formation. The leading wave had already overtaken the slide front at cavity collapse. Therefore the leading wave crest may be considered unaffected by the surface closure. The air pressure inside impact craters was measured by Abelson (1970) and the atmospheric pressure was altered experimentally by Gault and Sonett (1982). The analogy between explosion and landslide generated impact craters regarding cavity collapse and bore formation proposed by LeMéhauté and Wang (1995) suggests that the whole process of impulse wave generation by landslide impacts may be treated as incompressible. The detrainment of the landslide occurred during the final stages of the granulate deposition after the cavity collapse (Fig. 3Ae,f).

The velocity vector fields revealed the formation of a full saddle point in the water uplift (Fig. 3Bb,c). The full saddle propagated outward behind the leading wave crest and down to the channel bottom forming a half-saddle (Fig. 3Bd,e,f). The half-saddle marks the back of the leading wave crest where the water surface crosses the stillwater level. The saddle and half-saddles were characterized by instantaneously zero velocity. The largest velocities were measured locally around the slide front during slide penetration. The largest velocities in the wave field always occurred below the wave crests. The water particle velocity was only fractions of the shallow water wave velocity $(gh)^{0.5}$. The horizontal particle velocities were zero along vertical lines through the half-saddles, whereas the largest values were below the wave crest (Fig. 3C). The vertical particle velocities were zero along vertical lines through the wave crests (Fig. 3D). The largest values in the wave system were encountered at the location of the largest slope of the water surface. The vertical velocity in the jet issued by the rebound of the cavity collapse even exceeded the shallow water wave propagation velocity (Fig. 3De).

The in-plane divergence was roughly zero in the pure water flow area. Hence the fundamental assumption of the two-dimensional model was confirmed for the pure water flow area as determined by Fritz et al. (2003). Large

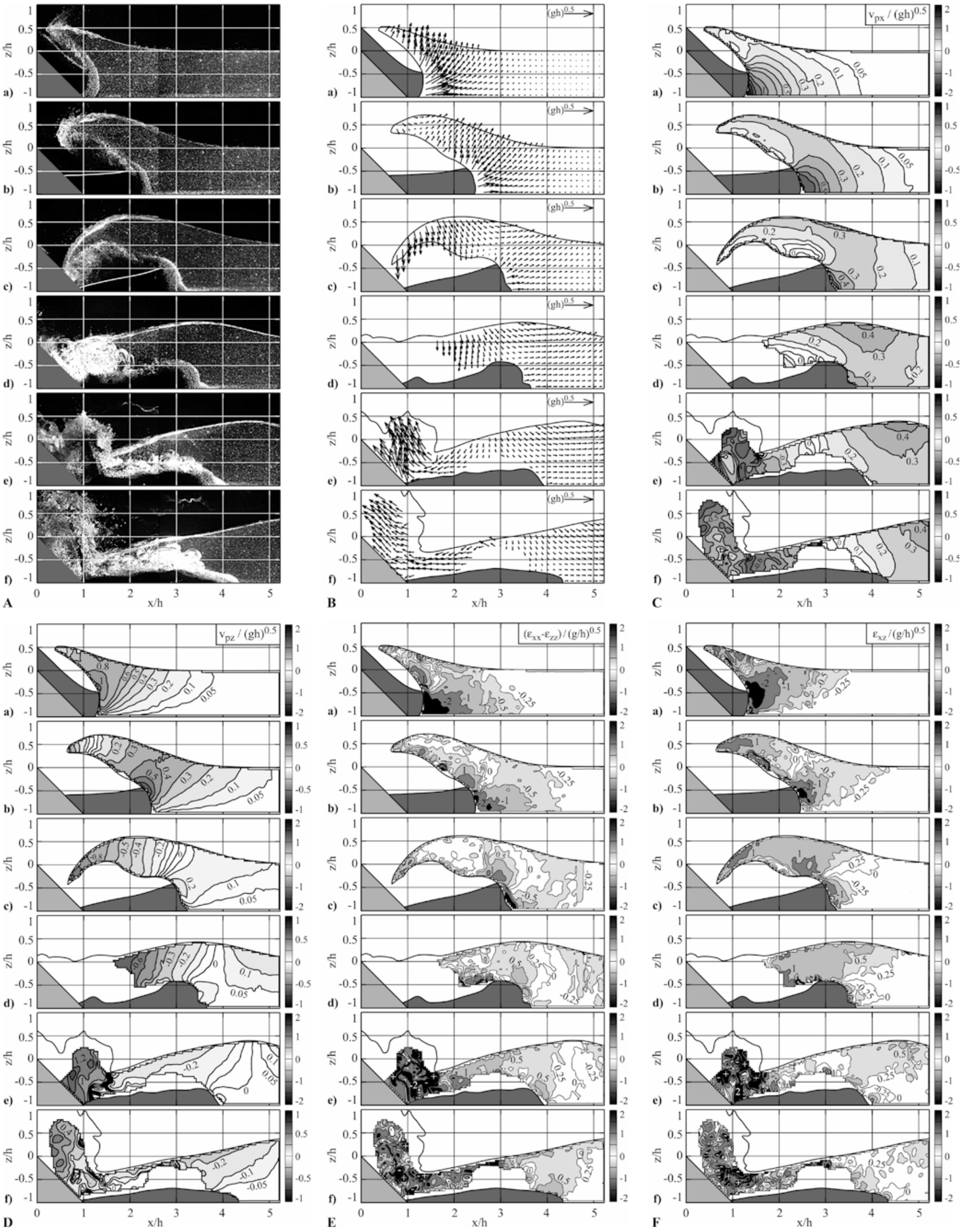
A
B
C
D
E
F
a)
b)
c)
d)
e)
f)
z/h
x/h
(gh)^0.5
v_px / (gh)^0.5
v_pz / (gh)^0.5
(ε_xx-ε_zz)/(g/h)^0.5
ε_xz/(g/h)^0.5
0
1
2
3
4
5
-1
-0.5
0.5

◄

Fig. 3. Backward collapsing impact crater: **A** PIV images of two mounted experiments at **F**=2.8, V=0.79, S=0.34, h=0.3 m and recorded at $t(g/h)^{0.5}$: *a* 0.72, *b* 1.48, *c* 2.24, *d* 3.01, *e* 3.77, *f* 4.53; **B** velocity vector fields; **C** horizontal particle velocity fields $v_{px}/(gh)^{0.5}$ with contour levels at 0, ±0.5, ±0.1, ±0.2, ±0.3, ±0.4, ±0.5, ±0.6, ±0.8, ±1, ±1.2, ±1.4, ±1.6, ±1.8, ±2; **D** vertical particle velocity fields $v_{pz}/(gh)^{0.5}$ with contour levels as in **C**; **E** elongational strain fields $(\epsilon_{xx}-\epsilon_{zz})/(g/h)^{0.5}$ with contour levels at 0, ±0.25, ±0.5, ±1, ±2; **F** shear strain fields $\epsilon_{xz}/(g/h)^{0.5}$ with contour levels as in **E**

divergence values were observed during the cavity collapse and the up-rise of the vertical jet (Fig. 3e,f). The cavity collapse and vertical jet formation was accompanied by a massive turbulent mixing of the three phases. The dark dots in the stem of the jet were granular grains swept along. The massive mixing process was three-dimensional and hence some out-of-plane motion may not be excluded. Further, the illumination patterns during the cavity collapse were dominated by the dark granular grains and the white air bubbles (Fig. 3Ae,f). Hence the correlation analysis likely locked in on the granular grains swept upward in the vertical jet rather than the seeding particles. The pure water flow below the outward propagating impulse waves was irrotational. The PIV data confirmed the assumption of irrotationality made by all analytical wave theories according to the Laplace equation. Significant vorticity was observed on the slide surface caused by the shear flow and in the mixing zone above the landslide deposit caused by the dissipative, three-dimensional turbulence.

The elongational and the shear strain fields are shown in Fig. 3E and F, respectively. The elongational strains were zero below wave crests and troughs because of the horizontal velocity vectors. The elongational strains were largest near the free surface at the locations of the largest gradients in the free surface. The largest negative elongational strains were computed in front of the penetrating landslide where the fluid cells were compressed along the horizontal x axis and expanded vertically (Fig. 3Ea,b,c). Analogously large negative elongational strains were measured in the upward shooting vertical jet (Fig. 3Ee). The maximum shear strain values in the wave field were always encountered below the wave crests. Both the elongational and the shear strain rates increased compared to the unseparated flow example presented in Fritz et al. (2003) because of the larger wave height.

3.4
Outward collapsing impact crater

A characteristic example at the lower end of the outward collapsing crater regime is shown in Fig. 4. The only difference to the previous example of a backward collapsing impact crater was a small increase in Froude number from **F**=2.8 to **F**=3.2. An example at the upper end of the outward collapsing crater regime with **F**=4.1 was presented in Fritz et al. (2003). The sets of figures include the original PIV images, the velocity vector fields, scalar fields of the velocity components, and contour plots of computed components of the deformation tensor. The selected sequence of original PIV recordings is shown Fig. 4A. The water flow around the penetrating landslide separated on the slide shoulder (Fig. 4Aa,b,c). The water was initially expelled upwards and outward by the entry of the landslide forming a water crater. The water crater exposed the ramp and the back of the landslide to the atmosphere. The displaced water volume obviously exceeded the landslide volume significantly. As the process of crater growth had terminated outward bulk motion of water was still present as a residuum. In contrast to the backward collapse no closure occurred in this case. The collapse occurred after the water crater reached its maximum size and the water rushed inwardly under the influence of gravity. The outward collapsing crater resulted in a main positive leading wave and negative base surge (Fig. 4Ad,e). The inrush of water filling the crater from downstream can qualitatively be viewed as an example of the classical dam break problem (Stoker 1957; Lauber 1997). The backward motion was initiated at the bottom of the crater wall where the hydrostatic pressure was the largest. The leading wave crest was issued by the crater rim and propagated outward during the crater collapse (Fig. 4Ac,d,e). The run-up of the base surge on the inclined ramp and the subsequent run-down formed the secondary wave system.

The velocity vector fields revealed the formation of a half-saddle in the water uplift (Fig. 4Bc,d,e). The half-saddle separated the outward from the inward flow. The largest velocities were measured locally around the slide front during slide penetration and in the splash. The water particle velocity below the wave crests was only fractions of the shallow water wave velocity $(gh)^{0.5}$, but increased compared to the previous examples because of the increase in wave height. The largest negative values of the horizontal velocity components were observed in the inward rush and run-up along the inclined ramp during the collapse of the impact crater (Fig. 4Cd,e). Negative vertical velocities were observed at the beginning of the crater collapse along the crater walls (Fig. 4Dc,d). Contrary to the classical dam break released from rest, the water displaced by the landslide at no instant reached a state near a static uplift. The kinetic energy of the landslide imparted on the water body was only partially converted into the potential energy of the uplift, whereas a significant part prevailed as kinetic energy in the form of the velocity field imposed onto the water body.

The computed in-plane divergence was roughly zero in the pure water flow area confirming the two-dimensional model assumption. Large divergence values were observed during the cavity collapse and the inward rush, which may be explained by the massive phase mixing, air compressibility, and the three-dimensional turbulence. The computed out-of-plane vorticity was roughly zero in the pure water flow below the outward propagating impulse waves. Hence the pure water flow was irrotational. Significant vorticity was observed on the slide surface caused by the shear flow and in the mixing zone above the landslide deposit caused by the dissipative turbulence.

The elongational and the shear strain fields are shown in Fig. 4E and F, respectively. The largest negative elongational strains were computed in front of the penetrating landslides were the fluid cells are compressed along the

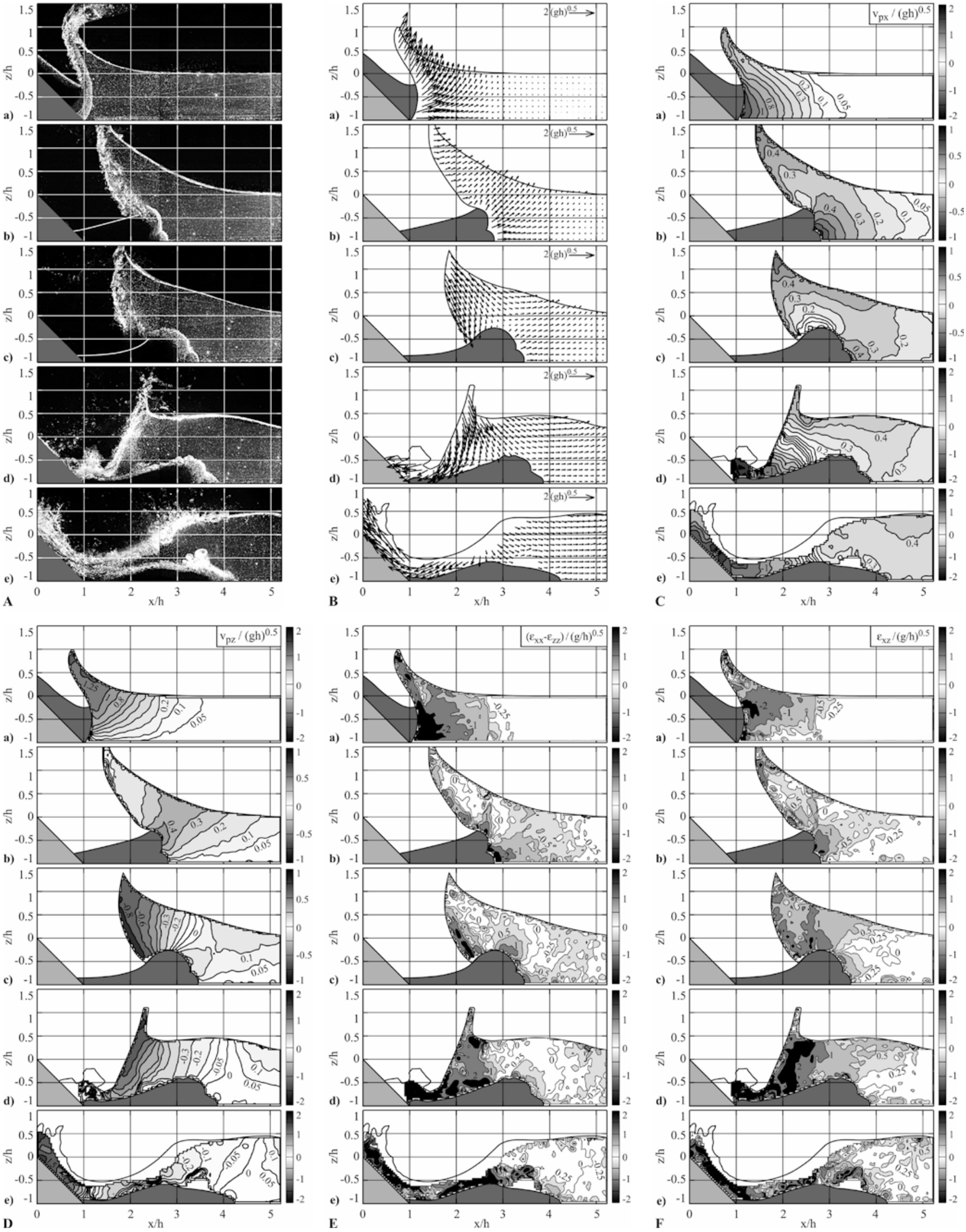
A
B
C
D
E
F
a)
b)
c)
d)
e)
z/h
x/h
$2(gh)^{0.5}$
$v_{px} / (gh)^{0.5}$
$v_{pz} / (gh)^{0.5}$
$(\varepsilon_{xx}-\varepsilon_{zz})/(g/h)^{0.5}$
$\varepsilon_{xz}/(g/h)^{0.5}$

◄

Fig. 4. Outward collapsing impact crater: **A** PIV images of two mounted experiments at **F**=3.2, *V*=0.79, *S*=0.31, *h*=0.3 m and recorded at $t(g/h)^{0.5}$: *a* 0.58, *b* 1.73, *c* 2.49, *d* 3.25, *e* 4.01; **B** velocity vector fields; **C** horizontal particle velocity fields $v_{px}/(gh)^{0.5}$ with contour levels at 0, ±0.5, ±0.1, ±0.2, ±0.3, ±0.4, ±0.5, ±0.6, ±0.8, ±1, ±1.25, ±1.5, ±2; **D** vertical particle velocity fields $v_{pz}/(gh)^{0.5}$ with contour levels as in **C**; **E** elongational strain fields $(\epsilon_{xx}-\epsilon_{zz})/(g/h)^{0.5}$ with contour levels at 0, ±0.25, ±0.5, ±1, ±2; **F** shear strain fields $\epsilon_{xz}/(g/h)^{0.5}$ with contour levels as in **E**

horizontal *x* axis and expanded vertically (Fig. 4E). Large positive elongational strains were measured during the crater collapse due to the stretching of the fluid cells along the *x* axis (Fig. 4Ed,e). Large positive shear strain values in the wave field were encountered in the crater rim during collapse and below the wave crests (Fig. 4Fc,d,e). In front of the slide negative shear strains were observed when the water was uplifted by the slide (Fig. 4F). Both the elongational and the shear strain rates increased compared to the previous examples because of larger wave heights.

4
Water displacement

4.1
Water displacement curves

The water displacement volume and rate were extracted from the PIV recordings. The area of the hump in the free surface could not be determined directly because the recordings did not reach far enough downstream in most cases. The water displacement volume V_d as a function of time was extracted from the PIV recordings specifying that the hump in the free surface had a volume about equal to the volume displaced by the landslide. The total crater volume corresponds to the combined slide and air volume below the still water surface. The definition of the water displacement volume V_d is shown in Fig. 5. This approach worked well for all cases in the separated flow regime. In the cases of unseparated flow at low slide impact velocities the task was difficult because of the flow through the granular medium as well as the air detrainment on the back of the slide resulting in a massive phase mixing in the wake of the landslide.

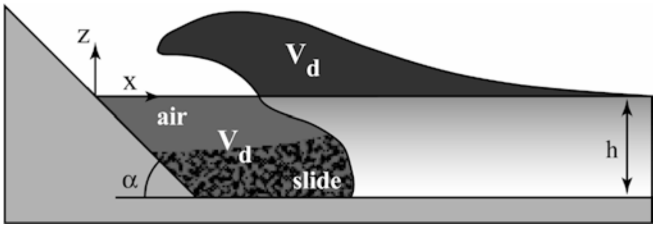

Fig. 5. Water displacement volume V_d corresponding to both the impact crater volume and the water volume under the hump above the stillwater level

The temporal evolution of the water displacement volume V_d was extracted from the PIV recordings of 34 mounted sets with different experimental parameters acquired at *h*=0.30 m and 0.45 m. Only separated flows were considered. In unseparated flows the water displacement volume can also exceed the landslide volume owing to the formation of a wave trough in the back of the slide. The water displacement volume in unseparated flows never exceeded the landslide volume by more than a factor of two. In these cases significant errors caused by the slide detrainment and the water flow through the slide granulate would lead to spurious results. Hence unseparated flows were not further analyzed. Both backward and outward collapsing impact craters were considered. By scaling the time after impact *t* with the time of the maximum displacement volume t_D and the water displacement volume V_d by the maximum water displacement volume V_D caused all of the displacement volume curves to collapse. The temporal evolutions of the normalized water displacement volumes V_d/V_D are shown in Fig. 6a. All curves exhibited a continuous increase of the water displacement volume V_d from the slide impact to the maximum displacement volume V_D. The decay after the maximum was relatively slow at the beginning because the landslides penetrated further into the water body as the impact craters were already collapsing. The water displacement estimates became noisier and finally broke down during the collapse of the impact craters because of the massive phase mixing caused either by the surface closure or the inward base surge. The accuracy in the determination of the water displacement volume V_d improved with increasing crater volume. The water displacement volumes were determined to ±5 %.

The water displacement volume as a function of time may be approximated by the empirical relationship

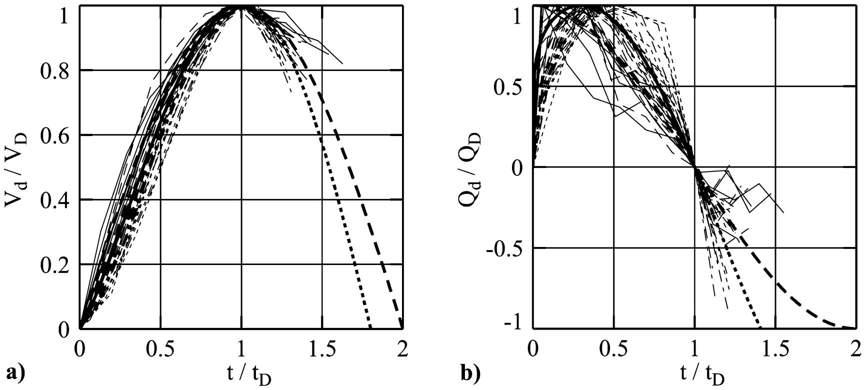

Fig. 6a, b. Normalized crater formation. **a** Water displacement V_d/V_D at: *solid curve*, 4<**F**<5; *long dashed curve*, 3<**F** ≤ 4; *long/short dashed curve*, 2.5<**F** ≤ 3; *short dashed curve*, 2<**F** ≤ 2.5 with *long dashed curve*, Eq. (4); *fat solid curve*, Eq. (5) at $t/t_D \leq 1$; *fat short dashed curve*, Eq. (5) at $t/t_D > 1$; **b** water displacement rate Q_d/Q_D with *fat long dashed curve*, Eq. (6); *fat solid curve*, Eq. (7) at $t/t_D \leq 1$; *fat short dashed curve*, Eq. (7) at $t/t_D > 1$; symbols as in **a**

proposed by LeMéhauté and Wang (1995) for water waves generated by underwater explosions

$$\frac{V_d}{V_D} = \sin\left(\frac{\pi}{2}\frac{t}{t_D}\right). \tag{4}$$

Underwater explosions and in particular nuclear blasts always exhibited the largest water displacement rate at $t/t_D=0$. The water displacement rate caused by a landslide reached the maximum roughly at $t/t_D=0.3$. The retarding effect may be explained by the strong compaction and deformation of the slide front on impact. Further, the landslides did not reach their maximum thickness at the front. Therefore the cross-section in contact with the water increased shortly after the impact. A slight modification of Eq. (4) allowing the initial retarding effect yields

$$\frac{V_d}{V_D} = \sin\left(\frac{\pi}{2}\left(\frac{t}{t_D}\right)^{\frac{3\pi}{8}}\right). \tag{5}$$

The impact crater volume expansion was described appropriately by Eq. (5), whereas the collapse remained uncertain. The water displacement volume could not be determined during the whole crater collapse. The landslide penetrated further into the water body increasing the water displacement locally at the beginning of the crater collapse. This suggests a slower decay in the water displacement volume than in craters produced by underwater explosions.

The temporal evolution of the water displacement rate was computed by differentiation of the water displacement curve. The temporal evolutions of the normalized water displacement rates Q_d/Q_D are shown in Fig. 6b. Scaling the time after impact with the time of the maximum displacement volume t_D and the water displacement rate Q_d by the maximum water displacement rate Q_D caused all of the displacement rate curves to collapse. The water displacement rate curves increased to the maximum rapidly and then decayed slower resulting in skewed curves. The accuracy of the water displacement rate estimates may be given to within ±20 %. Differentiation of Eq. (4) valid for underwater explosions and rescaling by the maximum displacement rate yields

$$\frac{Q_d}{Q_D} = \cos\left(\frac{\pi}{2}\frac{t}{t_D}\right) \tag{6}$$

with the normalized displacement rate Q_d/Q_D and the normalized time after impact t/t_D. Analogously differentiation of Eq. (5) valid for landslide impacts and simplification yields

$$\frac{Q_d}{Q_D} = \frac{9}{4\pi}\cos\left(\frac{\pi}{2}\left(\frac{t}{t_D}\right)^{\frac{3\pi}{8}}\right)\frac{3\pi^2}{16}\left(\frac{t}{t_D}\right)^{\frac{3\pi}{8}-1} \tag{7}$$

where the first factor on the right side rescales to the maximum displacement rate. The scattering of the measured water displacement rate curves is larger compared to those generated by underwater explosions (LeMéhauté and Khangoankar 1992). The curves below Eq. (7) in Fig. 6b corresponded to high velocity impacts of thick and short slides, whereas the curves above Eq. (7) represented slow and thin slides. The maximum water displacement rates of underwater explosions at the beginning of the detonation at $t/t_D=0$ are perfectly represented by Eq. (6). The maximum of Eq. (7) is located at $t/t_D=0.3$ matching the averaged time of the peak in the measured sets.

The empirical relationships Eqs. (5 and 7) representing the temporal evolutions of the water displacement volume V_d/V_D and the water displacement rates Q_d/Q_D, respectively, require only the determination of the maximum water displacement volume V_D, the maximum water displacement rate Q_D and the time after impact of the maximum displacement volume t_D. These quantities are discussed in the following paragraphs. The water displacement curves may be well suited as input curves for simplified numerical models. The water displacement curves are at the source, whereas the wave profiles are several water depths away from the source and therefore restricted by the two-dimensional model assumption. Use of the water displacement curves could help to define a source in numerical models without having to cope with the complexity of the subaqueous landslide motion, the flow separation, and the impact crater formation.

4.2
Maximum water displacement volume

The maximum water displacement volume V_D and the superimposed velocity field are of key importance regarding the whole wave generation process. The maximum water displacement volume was extracted from the water displacement curves shown in Fig. 6a. Only cases with flow separation were considered. The measured maximum water displacement volumes were within $1.8 \leq V_D/V_s \leq 8.1$ (below in Fig. 8a). Hence the dynamic water displacement volume always significantly exceeded the landslide volume V_s. The largest measured maximum water displacement per unit width was 8.1 times larger than the hydrostatic water displacement because of the added slide mass. The simple hydrostatic water displacement is not of relevance regarding landslide impacts for $\mathbf{F}\geq1$.Therefore the maximum water displacement volume V_D and not the slide volume V_s needs to be considered as relevant input quantity for initial conditions or uplifts in numerical models. The maximum water displacement volume of impacts without flow separation is expected to be within $1 \leq V_D/V_s \leq 2$. The asymptotic value $V_D/V_s=1$ may only be obtained by extremely slow landslide impacts at $\mathbf{F}\ll1$. The normalized maximum water displacement volume $V_D/(bh^2)$ may be related to the normalized time after impact $t_D(g/h)^{0.5}$ of the maximum water displacement volume by

$$\frac{V_D}{bh^2} = 0.39\left(t_D\sqrt{\frac{g}{h}}\right)^{2.1} \tag{8}$$

with an improved correlation coefficient $r^2=0.85$ (Fig. 7a). The normalized maximum water displacement volume $V_D/(bh^2)$ increased with the normalized duration from impact to the maximum displacement volume $t_D(g/h)^{0.5}$.

The predictive equation for the maximum water displacement volume $V_D/(bh^2)$ was determined by a multiple

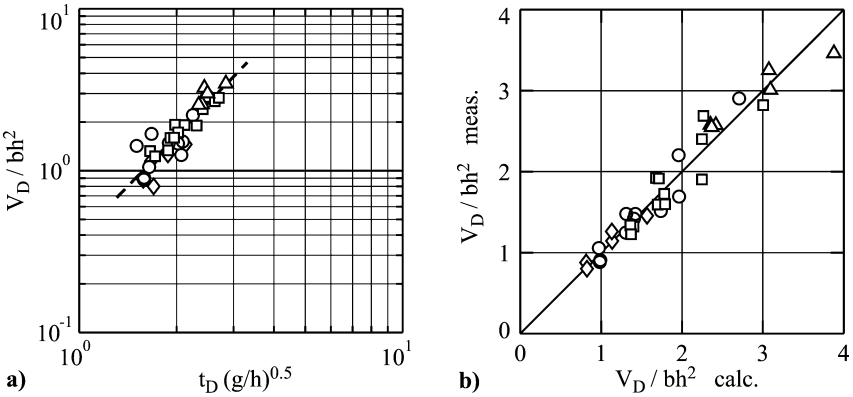

Fig. 7a, b. Maximum water displacement volume. **a** $V_D/(bh^2)$ vs. $t_D(g/h)^{0.5}$ with *dashed curve*, Eq. (8) and *open diamond*, $2<F \leq 2.5$; *open circle*, $2.5<F \leq 3$; *open square*, $3<F \leq 4$; *open triangle*, $4<F<5$; **b** $V_D/(bh^2)$ measured vs. $V_D/(bh^2)$ computed with Eq. (9) and symbols as in **a**

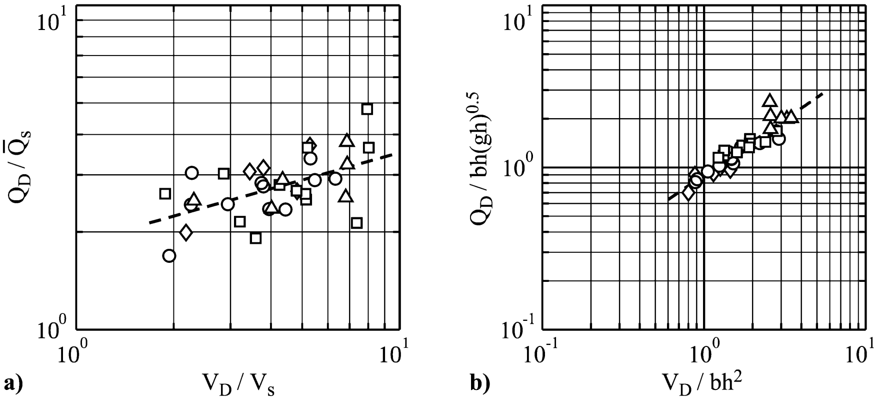

Fig. 8a, b. Maximum water displacement rate. **a**$Q_D/\bar{Q}_S$ vs. V_D/V_s with *dashed curve*, linear regression (r^2=0.30) and *open diamond*, $2<F \leq 2.5$; *open circle*, $2.5<F \leq 3$, *open square*, $3<F \leq 4$; *open triangle*, $4<F<5$; **b** $Q_D/(bh(gh)^{0.5})$ vs. $V_D/(bh^2)$ with Eq. (10) and symbols as in **a**.

regression of the measured values (Ratkowsky 1990). The slide Froude number $F = v_s/\sqrt{gh}$, the dimensionless slide volume $V_s/(bh^2)$, and the dimensionless slide thickness $S=s/h$ were used as parameters. A multiple regression for the water displacement volume yields

$$\frac{V_D}{bh^2} = 0.8\left(\frac{v_s}{\sqrt{gh}}\right)^1\left(\frac{V_s}{bh^2}\right)^{0.5} \tag{9}$$

with an excellent correlation coefficient r^2=0.93. The dominant dimensionless quantities are the slide Froude number F and the dimensionless slide volume V. Neglecting the slide thickness S had almost no effect on the correlation. The comparison between the measured values and predictions with Eq. (9) is shown in Fig. 7b. The largest deviations between the measured and the computed values were <15%.

4.3
Maximum water displacement rate

The maximum water displacement rate Q_D was extracted from the water displacement rate curves shown in Fig. 6b. The measured maximum water displacement rates $Q_D/\bar{Q}_S$ are shown in Fig. 8a. The maximum water displacement rate always exceeded the mean landslide inflow $\bar{Q}_S = V_s/t_{si}$ and the maximum slide inflow $Q_s=v_s sb$ with the channel width b. The duration of the slide impact t_{si} corresponds to the time from slide front impact until the rear end of the slide passed the imaginary still water surface. The normalized maximum water displacement rates were within $1.7 \leq Q_D/\bar{Q}_S \leq 4.8$ and $1 \leq Q_D/Q_s \leq 2.8$. Hence the dynamic water displacement rate can significantly exceed the landslide inflow. Therefore the maximum water displacement rate Q_D and not the slide inflow Q_s needs to be considered as relevant input quantity for wave maker boundary motions in numerical models. The maximum water displacement rate of impacts without flow separation may be $Q_D/Q_s \leq 1$. Maximum water displacement values $Q_D/Q_s<1$ are possible because of flow over the back of the landslide as well as a possible flow through the medium at extremely low slide velocities. The maximum water displacement rate may be related to the normalized maximum water displacement volume by

$$\frac{Q_D}{bh\sqrt{gh}} = 0.9\left(\frac{V_D}{bh^2}\right)^{2/3} \tag{10}$$

with an improved correlation coefficient r^2=0.79. The normalized maximum water displacement rate increased with the normalized maximum water displacement volume (Fig. 8b).

The predictive equation for the maximum water displacement rate was determined by a multiple regression with the relevant dimensionless quantities resulting in

$$\frac{Q_D}{bh\sqrt{gh}} = 0.6\left(\frac{v_s}{\sqrt{gh}}\right)^1\left(\frac{s}{h}\right)^{0.3} \tag{11}$$

with a good correlation coefficient r^2=0.85. The dominant dimensionless quantity is again the slide Froude number F. Contrary to Eq. (9) the dimensionless slide thickness S was the second parameter and not the dimensionless slide volume V, because the slide velocity together with the slide thickness determined the slide inflow rate. The

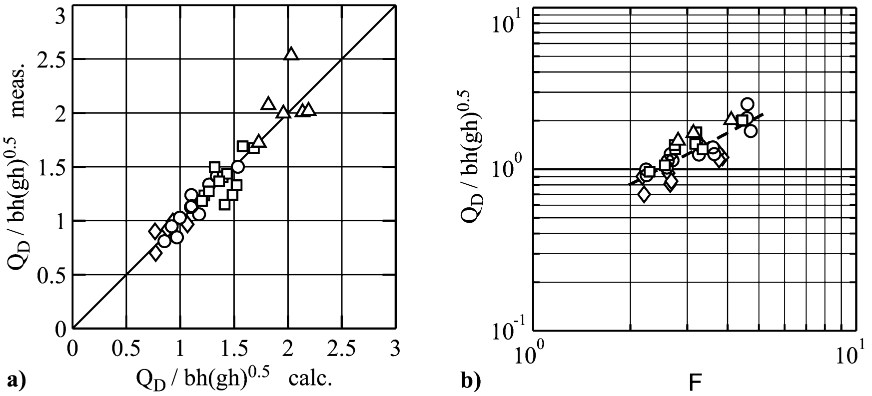

Fig. 9a, b. Maximum water displacement rate. **a** $Q_D/(bh(gh)^{0.5})$ measured vs. $Q_D/(bh(gh)^{0.5})$ computed Eq. (11), *open diamond*, $2<\mathbf{F}\le 2.5$; *open circle*, $2.5<\mathbf{F}\le 3$; *open square*, $3<\mathbf{F}\le 4$; *open triangle*, $4<\mathbf{F}<5$; **b** $Q_D/(bh(gh)^{0.5})$ vs. $\mathbf{F}=v_s/(gh)^{0.5}$ with *dashed curve*, linear regression ($r^2=0.67$); *open diamond*, $0<V\le 0.2$; *open circle*, $0.2<V\le 0.4$, *open square*, $0.4<V\le 0.8$; *open triangle*, $0.8<V<2$

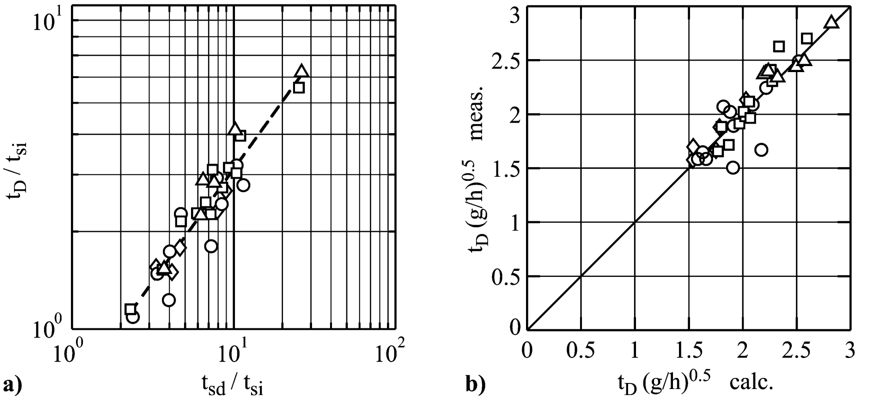

Fig. 10a, b. Duration of impact crater expansion. **a** t_D/t_{si} vs. t_D/t_{si} at *open diamond*, $2<\mathbf{F}\le 2.5$; *open circle*, $2.5<\mathbf{F}\le 3$; *open square*, $3<\mathbf{F}\le 4$; *open triangle*, $4<\mathbf{F}<5$ with *dashed curve*, Eq. (12); **b** $t_D(g/h)^{0.5}$ measured vs. $t_D(g/h)^{0.5}$ computed with Eq. (13) and symbols as in **a**

comparison between the measured values and the predicted ones computed with Eq. (11) is shown in Fig. 9a. The dependency of the maximum water displacement rate Q_D again on the slide Froude **F** number is shown in Fig. 9b.

4.4
Duration of impact crater expansion

The duration of the impact crater expansion corresponds to the time of the maximum water displacement volume t_D. The time of the maximum water displacement volume is of fundamental importance regarding the time scale of the whole wave generation process. The duration of the impact crater expansion was extracted from the water displacement curves shown in Fig. 6a. The normalized durations of the crater expansions t_D/t_{si} are shown in Fig. 10a. The duration of the crater expansion t_D may be related to the duration of the subaqueous slide motion t_{sd} by

$$\frac{t_D}{t_{si}} = 0.63\left(\frac{t_{sd}}{t_{si}}\right)^{0.7} \qquad (12)$$

with a correlation coefficient $r^2=0.90$. The duration of the slide impact t_{si} represents the duration from impact until the rear end of the slide passed the imaginary still water surface. The duration of the subaqueous slide motion t_{sd} corresponds to the timeframe from the impact to the deposit. The maximum water displacement volume always occurred after the whole slide mass had penetrated below the imaginary still water surface. The normalized times of the maximum water displacement volumes were within $1.1 \le t_D/t_{si} \le 6.2$. The duration of the impact crater expansion significantly exceeded the slide impact duration for short and thick slides, whereas for thin and elongated slides the duration of the impact crater expansion approached the slide impact duration. The maximum impact crater expansion represented by t_D was always reached well before the subaqueous slide motion was terminated at t_{sd}. The average value was $\overline{t_D/t_{sd}} = 0.45$ with a minimum of $t_D/t_{sd}=0.28$ and a maximum of $t_D/t_{sd}=0.7$. Hence the slide continued to run-out along the channel bottom while the impact crater was already collapsing. This suggests that the last part of the subaqueous slide motion was of secondary importance regarding the wave generation mechanism. A multiple regression of the dimensionless parameter t_D/t_{sd} with all three dimensionless quantities **F**, V, and S yielded a poor correlation coefficient. Hence the time of the slide motion t_{sd} from the impact to the deposit is an ill-defined time normalization parameter.

The best multiple regression for the duration of the impact crater expansion $t_D(g/h)^{0.5}$ yields

$$t_D\sqrt{\frac{g}{h}} = 1.7\left(\frac{v_s}{\sqrt{gh}}\right)^{0.3}\left(\frac{V_s}{bh^2}\right)^{0.2} \qquad (13)$$

with a correlation coefficient $r^2=0.75$. The dominant dimensionless quantities are the slide Froude number **F** and the dimensionless slide volume V. Neglecting the slide thickness S had only a minor effect on the correlation coefficient. The comparison between the measured values and predictions computed with Eq. (13) is shown in Fig. 10b.

4.5
Time of maximum displacement rate

The time of the maximum water displacement rate t_{qD} was extracted from the water displacement curves shown in Fig. 6b. The normalized times of the maximum water displacement rates $t_{qD}(g/h)^{0.5}$ and t_{qD}/t_D are shown in Fig. 11a and b, respectively. The measurements of t_{qD} were disturbed by a high noise level resulting in a broad scattering of the data. The maximum water displacement rate occurred before the collapse of the impact crater was initiated. The measurements of the maximum water displacement rates were within $0.05 \le t_{qD}/t_D \le 0.6$ and on average at $t_{qD}/t_D = 0.3$. Relative to the duration of the slide impact, the maximum water displacement rates were recorded at $0.1 \le t_{qD}/t_{si} \le 1.25$ with an average of $t_{qD}/t_{si} = 0.7$. Hence the maximum water displacement rate was reached either before the back of the slide had penetrated the imaginary still water surface or just thereafter. For comparison underwater explosions always generated the largest water displacement rates at the detonation with t_{qD}=0 (LeMéhauté and Wang 1995). The landslides built up their water displacement rate with increasing slide thickness during the slide penetration. In addition, the strong compaction and deformation of the slide front at impact was responsible for a certain retarding effect. Therefore the water displacements produced by landslide impacts are more difficult to treat analytically than those generated by underwater explosions.

The predictive equation for the time of the maximum water displacement rate $t_{qD}(g/h)^{0.5}$ yields

$$t_{qD}\sqrt{\frac{g}{h}} = 2.2\left(\frac{v_s}{\sqrt{gh}}\right)^{-1.6}\left(\frac{V_s}{bh^2}\right)^{0.6}\left(\frac{s}{h}\right)^{-0.8} \qquad (14)$$

with a weak correlation coefficient r^2=0.38. The temporal determination of the maximum water displacement rate was fuzzy because of the uncertainty in the estimates and the time increment of the recordings. The multiple regression for the time of the maximum water displacement rate t_{qD} normalized by the duration of the crater expansion t_D yields

$$\frac{t_{qD}}{t_D} = 1.4\left(\frac{v_s}{\sqrt{gh}}\right)^{-2}\left(\frac{V_s}{bh^2}\right)^{0.5}\left(\frac{s}{h}\right)^{-0.9} \qquad (15)$$

with a similar correlation coefficient r^2=0.45 as Eq. (14). The comparisons between the measured values and predictions computed with Eqs. (14 and 15) are shown in Fig. 11a and b, respectively. The broad scattering was due to the uncertainties involved in the estimates and the limited determination of t_{qD}. The relationship given by Eq. (14) is recommended to predict the time of the maximum water displacement rate t_{qD}, because Eq. (15) requires the determination of the duration of the crater expansion t_D beforehand.

5
Conclusions

The initial phase of landslide generated impulse waves in reservoirs, lakes, bays, or oceans was investigated in a two-dimensional physical laboratory model based on the generalized Froude similarity. Landslides were successfully modeled with an artificial granular material consisting of barium sulfate and polypropylene (PP-$BaSO_4$). By use of the pneumatic landslide generator that was developed, the slide impact characteristics could be controlled, thus allowing exact reproduction and independent variation of single dynamic slide parameters. The results of this experimental study regarding the hydrodynamic impact craters of the slide impact and the extracted water displacements may be summarized as follows:

- The macro-structure of the flow in the impact and wave generation area was determined with PIV. Mounted areas of view resulted in 49 flow map sequences covering 1.6 m×0.8 m. The following flow maps were computed: velocity vector, streamline, absolute velocity, horizontal and vertical particle velocity, in-plane divergence, out-of-plane rotation, and elongational and shear strain rate.
- The in-plane divergence was roughly zero in the pure water flow area confirming the two-dimensional model assumption. Out-of-plane motion was observed in the wake of the slide and the massive phase mixing area.
- A flow separation criteria based on the slide Froude number **F** and the dimensionless slide thickness *S* was used to distinguish between separated and unseparated flow regimes in the impact and wave generation area. In the separated flow regime an impact crater forms.
- In the separated flow regime two types of impact craters were defined based on the slide Froude number **F** and

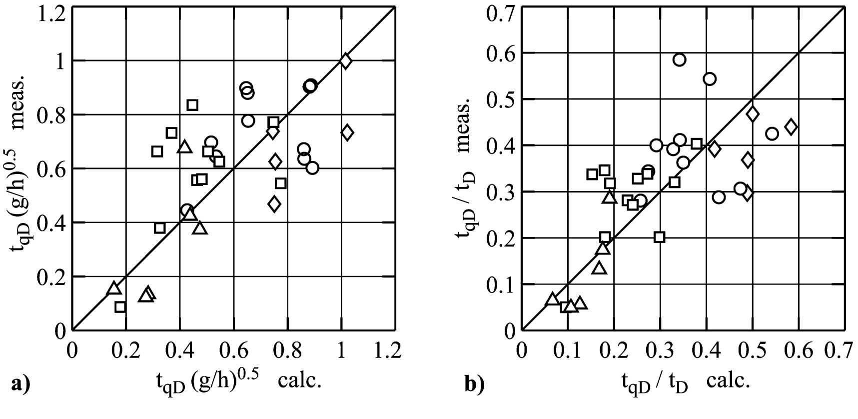

Fig. 11a, b. Time of maximum displacement rate. **a** $t_{qD}(g/h)^{0.5}$ measured vs. $t_{qD}(g/h)^{0.5}$ computed with Eq. (14), *open diamond*, 2<**F** ≤ 2.5; *open circle*, 2.5<**F** ≤ 3; *open square*, 3<**F** ≤ 4; *open triangle*, 4<**F**<5; **b** t_{qD}/t_D measured vs. t_{qD}/t_D computed with Eq. (15), symbols as in **a**

the dimensionless slide thickness *S*. The backward collapsing impact crater was characterized by a surface closure during crater collapse forming an air cavity, whereas in the outward collapsing impact crater no cavity was formed.

- A static departure from the still water surface was not observed. Water particle velocities were present in the flow field at all instants in time. A velocity field needs to be superimposed on a free surface disturbance as initial condition for numerical simulations.
- The temporal evolution of the water displacement volume and rate were fully described in terms of the time of the maximum water displacement, the maximum water displacement volume and rate.
- The time of the maximum water displacement, the maximum water displacement volume and rate were determined by multiple regressions. The slide Froude number **F** was identified as the dominant parameter.
- The maximum water displacement volume always exceeded the landslide volume. The largest measured maximum water displacement per unit width was eight times larger than the hydrostatic water displacement because of the added slide mass. The simple hydrostatic water displacement is not of relevance regarding landslide impacts for $\mathbf{F}\geq 1$.
- The volume and rate of the water displacement determined herein may allow a coupling of the physical model results with numerical models close to the source resulting in hybrid models. Further, the water displacement curves may lead to a substitution of the highly complex coupling between the mass flow and the water body by a simplified numerical model.

References

Abelson HI (1970) Pressure measurements in the water-entry cavity. J Fluid Mech 44:129–144

Birkhoff T, Zarantonello FH (1957) Jets, wakes and cavities. Academic Press, New York

Fritz HM, Hager WH, Minor H-E (2001) Lituya Bay case: rockslide impact and wave run-up. Sci Tsunami Hazards 19:3–22

Fritz HM (2002a) PIV applied to landslide generated impulse waves. In: Adrian RJ et al. (eds) Laser techniques for fluid mechanics. Springer, New York Berlin Heidelberg, pp 305–320

Fritz HM (2002b) Initial phase of landslide generated impulse waves. Ine Minor H-E (ed) VAW Mitteilung 178. Versuchsanstalt für Wasserbau, Hydrologie und Glaziologie, ETH Zürich

Fritz HM, Moser P (2003) Pneumatic landslide generator. Int J Fluid Power 4:49–57

Fritz HM, Hager WH, Minor H-E (2003) Landslide generated impulse waves, part 1: Instantaneous flow fields. Exp Fluids http://dx.doi.org/10.1007/s00348-003-0659-0

Gault DE, Sonett CP (1982) Laboratory simulation of pelagic asteroidal impact: atmospheric injection, benthic topography, and the surface wave radiation field. In: Silver LT, Schultz PH (eds) Geological implications of impacts of large asteroids and comets on the earth. Geol Soc Am Spec Pap 190:69–92

Holst M (1977) Underwater explosions. Ann Rev Fluid Mech 9:187–214

Huber A (1980) Schwallwellen in Seen als Folge von Bergstürzen. In: Vischer D (ed) VAW Mitteilung 47. Versuchsanstalt für Wasserbau, Hydrologie und Glaziologie, ETH Zürich (in German)

Lauber G (1997) Experimente zur Talsperrenbruchwelle im glatten geneigten Rechteckkanal. In: Vischer D (ed) VAW Mitteilung 152. Versuchsanstalt für Wasserbau, Hydrologie und Glaziologie, ETH Zürich (in German)

Lee M, Longoria RG, Wilson DE (1997) Cavity dynamics in high-speed water entry. Phys Fluids 9:540–550

LeMéhauté B, Khangoankar T (1992) Generation and propagation of explosion generated waves in shallow water. Technical Report DNA-TR-92–40, Defense Nuclear Agency, Washington DC

LeMéhauté B, Wang S (1995) Water wave generated by underwater explosions. In: Advanced series on ocean engineering, vol 10. World Scientific, Singapore

Liggett JA (1994) Fluid mechanics. McGraw-Hill, New York

Müller D (1995) Auflaufen und Überschwappen von Impulswellen an Talsperren. In: Vischer D (ed) VAW Mitteilung 137. Versuchsanstalt für Wasserbau, Hydrologie und Glaziologie, ETH Zürich (in German)

Raffel M, Willert CE, Kompenhans J (1998) Particle image velocimetry—a practical guide. Springer, Berlin Heidelberg New York

Ratkowsky DA (1990). Handbook of nonlinear regression models. Statistics: textbooks and monographs, vol 107. Dekker, New York

Scarano F, Riethmuller ML (2000) Advances in iterative multigrid PIV image processing. Exp Fluids 29:S51–S60

Slingerland RL, Voight B (1979) Occurrences, properties and predictive models of landslide-generated impulse waves. Rockslides and avalanches, 2. In: Voight B (ed) Developments in geotechnical engineering, vol 14B. Elsevier, Amsterdam, 317-397

Stoker JJ (1957) Water waves. Interscience, New York

Vischer DL, Hager WH (1998) Dam hydraulics. Wiley, Chichester